Article

Influence of the Projectile Rotation on the Supersonic Fluidic Element

Yufang Wang [1] and Nannan Wang [2,*]

[1] AVIC Changcheng Institute of Metrology and Measurement, Beijing 100095, China
[2] Department of Aerospace Engineering, Beijing Institute of Technology, Beijing 100081, China
* Correspondence: 18811360596@163.com

Abstract: The effects of projectile rotation on the internal and external flow fields of the supersonic fluidic element are numerically studied using sliding grid technique and the RNG k-ε turbulence model. The effects of rotating speed on internal and external flow fields, switching time and output characteristics are studied. The results show that: for the external flow field, there is no obvious change in the flow field structure at low angular velocity; when the angular velocity increases to 20 r/s, the flow field structure becomes obviously asymmetric due to the Coriolis force; the flow field far away from the surface of the projectile body (more than 0.3 m) is much more affected than the flow field near the surface of the projectile body. The influence of projectile rotation on the internal flow field is much weaker than on the external flow field, and the change of internal flow field is not obvious when the rotational speed is less than 20 r/s. The switching time decreases with the increase in angular velocity, and within normal range of the angular velocity, the deviation of switching time from that without rotation is within 5%. The change of thrust distribution is not obvious when the rotational speed is less than 20 r/s. However, when the rotational speed reaches 50 r/s, the thrust of the middle part of the right nozzle increases by about 20 N.

Keywords: numerical simulation; turbulence model; fluidic element; computational fluid dynamics

Correction Statement: This article has been republished with a minor change. The change does not affect the scientific content of the article and further details are available within the backmatter of the website version of this article.

1. Introduction

The fluidic element is a kind of fluid control device with fluid as working medium and no moving parts, also known as a fluid amplifier, which can act as the logic element or executive component in the control system. Compared with semiconductor amplifier devices, fluidic components have higher reliability in complex mechanical and electromagnetic environments. The fluidic element has many kinds, of which the wall-attached fluidic element is the most commonly used. The wall-attached fluidic element works according to the wall attachment effect of the jet (Coanda effect) and generally has two stable working states. Supersonic fluidic element refers to a fluidic element with supersonic gas as working medium. The current development direction for supersonic fluidic elements mainly includes: (1) the application of supersonic fluidic elements in the attitude control of the flight vehicle [1]; (2) the application of the supersonic fluidic element as ultrasonic generator in air-coupled ultrasonic testing [2–5]; and (3) the application of oscillating supersonic fluidic elements (also called supersonic fluidic oscillators) in flow control and air-fuel mixing [6,7].

In the rocket projectile angle stability control system, the supersonic fluidic element can act as a last-stage power amplifier and actuator. Under the control of low-power pneumatic signals, it causes the high-power supersonic jet to deflect. Under the guidance of special flow channels, it causes the thrust vector of the jet to change with the change of the control signal. This thrust vector acts on the missile and corrects the flight attitude deviation of the missile in real time, as shown in Figure 1.

The working mechanism of the supersonic fluidic element is as follows. The high-pressure airflow which forms the gas source is accelerated by a Laval nozzle to generate a

supersonic jet. Under the effect of the left and right control flows with different flow rates, the supersonic jet deflects to one side and forms a stable wall-attaching flow until it ejects from one side of the outlet, generating a control force perpendicular to the axis direction of the supersonic fluidic element, which constitutes a control moment relative to the center of mass of the rocket. The control moment prevents the longitudinal axis of the rocket from deviating from the given fire direction, so as to reduce the dispersion of the impact point. The direction of control force can be changed by changing the flow rates of the left and right control ports.
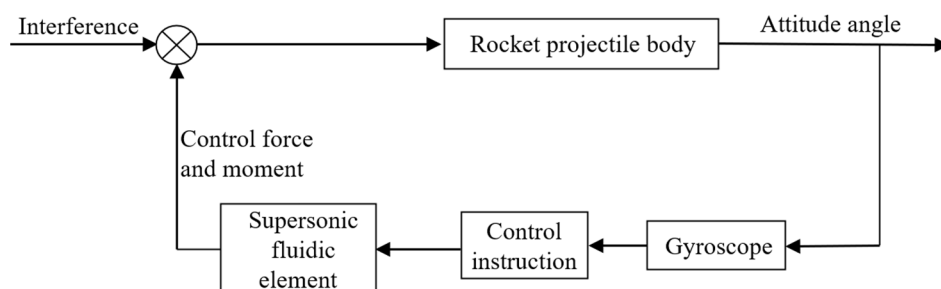
Figure 1. Working principle of the rocket attitude control system.

There are four supersonic fluidic elements distributed in the rocket attitude control system, as shown in Figure 2b. They are divided into two groups that are perpendicular to each other, where I and III are one group, and II and IV are the other group. They work alternately according to the control command to control the yaw and pitch flight attitude of the rocket in real time. The eight rectangular gas jet nozzles are uniformly distributed along the circumference near the head of the rocket, as shown in Figure 2a. According to the PWM control signal, the angle stabilization system works within a certain range of the active section. When each group of supersonic fluidic elements works, they will form a lateral control force in two mutually perpendicular channels. The direction of the average control force is always generated according to the need to reduce the angular velocity and deflection angle of the missile axis, so as to achieve the goal of attitude stabilization.

The internal flow field structure and switching mechanism of fluidic elements have been extensively studied. Uwe Reisch and Rosemarie Meuer [8] numerically simulated the flow of two-dimensional supersonic jet elements with the CFD method, and they pointed out that the choice of turbulence model would affect the prediction results of separation point positions. Bai Yalei and Mingxiao [9] studied the velocity distribution, pressure distribution and the unsteady flow mechanism of the internal flow field of a wall-attached fluidic element. The results show that the deflection of the main jet is caused by the pressure difference on both sides of the main jet, and the low-pressure eddy induces the main jet to attach to the wall. Roger R and Chan S [10] conducted a numerical simulation study on single-stage and two-stage bistable fluid amplifiers. Wang, N. et al. [11,12] studied the wall-attached flow characteristic and the flow structure in the output channel of supersonic fluidic elements under different inlet pressures. T Murao and K Sudou [13] analyzed the velocity distribution and streamline mode in the fluidic element through numerical simulation, and they analyzed the switching mechanism using the predicted stream function. Xu Yong et al. [14–20] studied the mechanism of steady flow, unsteady flow and switching in supersonic jet elements by numerical method. The influence of inlet and outlet flow parameters on the dynamic performance of supersonic jet elements was studied in detail through numerical simulation. It was found that increasing the mass flow rate of control flow can shorten the switching time and slightly increase the effective thrust, but also weaken the stability of wall-attached flow and energy utilization. The numerical results showed that the instability of the main vortex center was the main reason for the fluctuation of the output thrust. The vortex structures at different switching times were calculated and analyzed. The switching process of supersonic jet elements was found to be

an extremely complex process, including complex shock wave system evolution, free shear layer, boundary layer evolution and multi-vortex instability evolution.
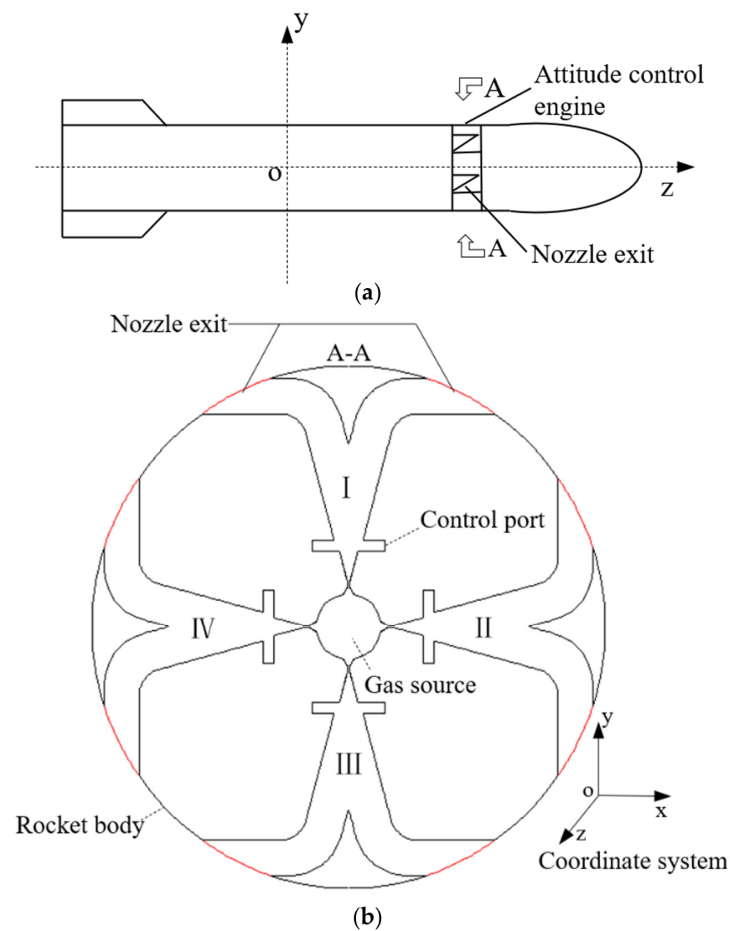
Figure 2. Position (**a**) and structure (**b**) of supersonic fluidic element on rocket.

Many researchers have also studied the influence of relevant parameters on the performance of jet elements. Sun Na et al. [21] studied the main channel parameters that affect the switching performance of light-small fluidic elements. The results showed that the control diameter, expansion diameter and split distance had a greater influence on the switching performance, while the expansion half angle had no significant influence on switching performance. Peng J M et al. [22,23] studied the influence of actuator parameters and geometric parameters on the critical velocity of a fluid amplifier in a liquid jet hammer through numerical and experimental studies. The results show that each geometric parameter has a significant influence on the critical velocity, and the consistency between simulation and measurement is considered to be completely acceptable. When the piston diameter is less than a certain value, increasing the piston diameter will rapidly reduce the critical flow rate. When the diameter of the piston rod is greater than a certain value, the critical flow rate increases rapidly, and it increases almost linearly with the mass of the impactor and has nothing to do with the stroke length of the impactor.

In addition, the modeling, testing and design methods of fluidic components have also been studied. Peng Z and Yao X [24] established a dynamic mathematical model of the fluidic element in the form of nonlinear differential equations, simulated and analyzed the piston movement during the switching process of the fluidic element, studied the factors affecting the switching characteristics, and carried out experimental verification. Zhang ZB and Wu Ju MA [25] designed a real-time test method for the switching time of fluidic elements. A Hall sensor was used to detect the position of a rocker arm to test the switching time of jet force, and modeling and simulation were carried out. Wuju MA et al. [26]

analyzed the influence of the jet force switching delay time of the fluidic element on the precision of a rolling guidance rocket by establishing the mechanical model of the guided rolling rocket.

In order to eliminate the influence of thrust eccentricity, aerodynamic eccentricity and other factors, the long-range rocket projectile generally adopts the rotating body system, and the rotating angular velocity is usually 5~20 r/s. The designers of rocket control systems are most concerned about whether and how the rotation of the projectile affects the output characteristics of supersonic fluidic elements, such as control force and switching characteristics. The projectile rotation has certain influence on the output characteristics of the fluidic element. Firstly, the projectile rotation will cause the jet and thrust vector of the supersonic fluidic element to appear in the form of rotation. Secondly, the internal flow mechanism of the supersonic fluidic element will also be affected by the centrifugal force and Coriolis force caused by the projectile rotation. In order to analyze and design the attitude control system accurately, it is necessary to quantify the effect of projectile rotation on the performance of supersonic fluidic elements.

As far as the authors know, in the literature there are no systematic papers in which focus on the study of the influence of projectile rotation on the fluidic element. In this paper, the changes of internal and external flow fields caused by projectile rotation are numerically investigated to guide the development and improvement of supersonic fluidic elements. The work of this paper is divided into three parts: (1) research on the influence of projectile rotation on the external jet flow of a single supersonic fluidic element; (2) research on the influence of projectile rotation on the external control jet flow of two supersonic fluidic elements working simultaneously; and (3) study of the influence of projectile rotation on the internal and external flow fields of supersonic fluidic elements.

2. Materials and Methods

2.1. Flow Controlling Equations

Experimental study and theoretical analysis show that the internal flow field of a supersonic jet element is turbulent flow with shock wave and flow separation. Theoretically, the direct numerical simulation of the N-S equations is required in order to accurately simulate the turbulent flow details in the supersonic fluidic element. Due to the complexity of turbulent flow, direct numerical simulation requires huge computation workload and is difficult to achieve at present. The Reynolds average method is widely used in engineering to simulate turbulent flow. The Reynolds averaged method uses the RANS (Reynolds averaged N-S) equation as the control equation. The physical quantities in the turbulent flow field are decomposed into the time averaged term and the pulsating term. The time averaged term describes the average effect of turbulence, and the pulsating term describes the transient fluctuations of turbulence. Although the RANS equation cannot reflect the complex coherent structure of turbulence, its calculation amount is greatly reduced, and its accuracy and reliability have been tested by practice. At present, using RANS equations in combination with the turbulence model is the main method to solve the viscous flow problem of fluidic elements in engineering.

The compressible Reynolds average N-S equations are adopted as the flow controlling equations, which can be written as [27]:

$$\begin{cases} \dfrac{\partial \rho}{\partial t} + \dfrac{\partial}{\partial x_i}(\rho u_i) = 0 \\[2mm] \dfrac{\partial}{\partial t}(\rho u_i) + \dfrac{\partial}{\partial x_j}(\rho u_i u_j) = -\dfrac{\partial p}{\partial x_i} + \dfrac{\partial \tau_{ij}}{\partial x_j} + \dfrac{\partial \tau_{ij}^t}{\partial x_j} \\[2mm] \dfrac{\partial}{\partial t}(\rho E) + \dfrac{\partial}{\partial x_i}[u_i(\rho E + p)] = \dfrac{\partial}{\partial x_j}\left(u_i \tau_{ij} + u_i \tau_{ij}^t\right) + \dfrac{\partial}{\partial x_i}\left(q_i + q_i^t\right) \end{cases} \tag{1}$$

where ρ is average density; p is average static pressure; u is average velocity; E is the average internal energy density; τ_{ij} is the average viscous stress; τ_{ij}^t is the Reynolds stress; q_i is the average heat flux; and q_i^t is the turbulent heat flux.

The average viscous stress τ_{ij} can be expressed as

$$\tau_{ij} = -\mu \left(2S_{ij} - \frac{2}{3}\frac{\partial u_k}{\partial x_k}\delta_{ij} \right) \tag{2}$$

where μ is the viscosity coefficient, and S_{ij} is the average rate of strain. Reynolds stress τ_{ij}^t can be expressed as

$$\tau_{ij}^t = -\mu_t \left(2S_{ij} - \frac{2}{3}\frac{\partial u_k}{\partial x_k}\delta_{ij} \right) \tag{3}$$

where μ_t is the eddy viscosity coefficient. The average rate of strain S_{ij} can be expressed as

$$S_{ij} = \frac{1}{2}\left(\frac{\partial u_j}{\partial x_i} + \frac{\partial u_i}{\partial x_j} \right) \tag{4}$$

The average heat flux q_i can be expressed as

$$q_i = -\lambda\frac{\partial T}{\partial x_i} \tag{5}$$

where λ is the thermal conductivity, and T is the average temperature. The turbulent heat flux q_i^t can be expressed as

$$q_i^t = -\lambda_t\frac{\partial T}{\partial x_i} \tag{6}$$

where λ_t is the turbulent conductivity.

The average internal energy density E can be expressed as

$$E = \frac{p}{(\gamma - 1)\rho} + \frac{1}{2}(u_i u_i) \tag{7}$$

In order to close the equations, it is also necessary to add the gas equation of state. For compressible flow, the form of the ideal gas law is:

$$\rho = \frac{p}{RT} \tag{8}$$

where p is the static pressure, and R is the gas constant.

2.2. Turbulence Model

Turbulence models are some specific relations that relate the additional term of turbulence fluctuation value with the time mean value. This paper adopts the RNG k-ε turbulence model [28], which is suitable for numerical simulation of jet and rotation flow and can be expressed as:

$$k = \frac{1}{2}(u_i' u_i') \tag{9}$$

$$\varepsilon = C_D\frac{k^{3/2}}{l} \tag{10}$$

$$\mu_t = C_\mu\rho\frac{k^2}{\varepsilon} \tag{11}$$

$$\rho\frac{\partial k}{\partial t}\rho u_i\frac{\partial k}{\partial x_i} = (\frac{\partial}{\partial x_i})[(\mu_1 + \frac{\mu_t}{\sigma_k})\frac{\partial k}{\partial x_i}] + G - \rho\varepsilon \tag{12}$$

$$\rho\frac{\partial\varepsilon}{\partial t} + \rho u_j\frac{\partial\varepsilon}{\partial x_j} = (\frac{\partial}{\partial x_j})[(\mu_1 + \frac{\mu_t}{\sigma_\varepsilon})\frac{\partial\varepsilon}{\partial x_j}] + C_1 G\frac{\varepsilon}{k} - C_2\rho\frac{\varepsilon^2}{k} \tag{13}$$

$$G = [\mu_t(\frac{\partial\mu_i}{\partial x_j}) + \mu_t(\frac{\partial\mu_j}{\partial x_i}) - \frac{2}{3}\delta_{ij}\rho k] \cdot \frac{\partial\mu_i}{\partial x_j} \tag{14}$$

where u' is fluctuation velocity; k is the turbulent pulsating kinetic energy of unit mass fluid; ε is the dissipation rate of pulsating kinetic energy of unit mass fluid in turbulence flow, that is, the rate at which the mechanical energy of isotropic small-scale vortex is converted into heat energy; and G is the turbulent flow energy generation term.

2.3. Geometric Models, Boundary Conditions and Computational Grids

According to the working characteristics of supersonic fluidic elements and the specific conditions, the geometric model is simplified to 2D. Figure 3 shows the geometry model and boundary conditions of the external flow field of a single jet ejecting from the nozzle exit, where the rotation axis passes the origin o in a vertical direction, and the projectile rotates in a counterclockwise direction. To ensure the full development of the jet ejected from the nozzle exit, the far field radius (R) is taken as ten times the projectile radius (r). The area near the nozzle is marked as Zone I, and the other part is marked as Zone II. Structured grids are generated in the computational domain, as shown in Figure 4. The grid near the nozzle and on the wall is densified according to the actual flow. In the calculation process, the grid is optimized in real time according to the current flow situation every 1000 iteration steps, making it more in line with the needs of the flow field.

The boundary conditions are as follows: the nozzle exit is set as the velocity inlet; the turbulent kinetic energy at the inlet is 1% of the average kinetic energy of the incoming flow; pressure far field conditions are given for outer boundary; isothermal wall assumption and no slip boundary condition are adopted on the solid wall of the projectile.

In actual operation of the attitude control engine, two supersonic fluidic elements work at the same time to provide two parallel jets in the same direction. Figure 5 is a schematic diagram of the geometric model of the two parallel jets. The geometry model, computational grids and boundary conditions of the simulation of two parallel jets are basically the same as that of a single jet, except that there is an additional nozzle exit.
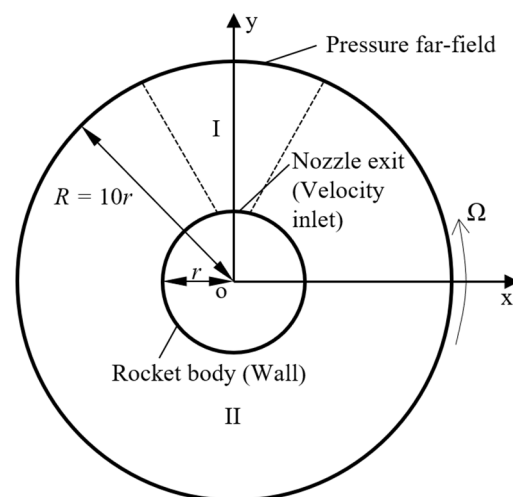
Figure 3. Computational domain and boundary conditions.

Figure 6 shows the geometric model of the internal and external flow fields of a supersonic jet element. The sliding grid technology is used to simulate the rotating flow field, and the computational domain is divided into two independent parts. The two parts of the grid are interpolated through the sliding interface. Figure 7 shows the computational grid of the internal and external flow fields. The gas source is set as the pressure inlet with

total pressure of 2 MPa, the control ports are set as the mass flow inlet in which the left and right mass flow rates are 0.1 kg/s and 0.003 kg/s, respectively, and other boundary settings are the same as above.
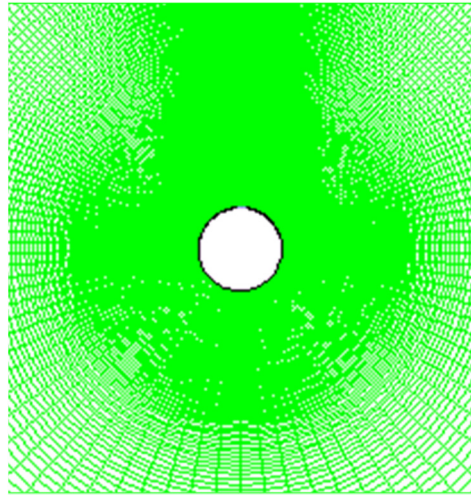
Figure 4. Computational grid.
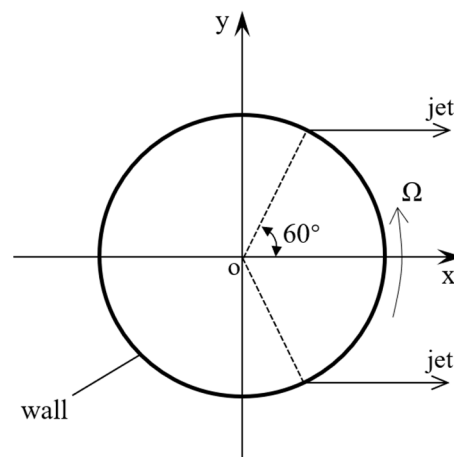
Figure 5. Geometric model of parallel jets.
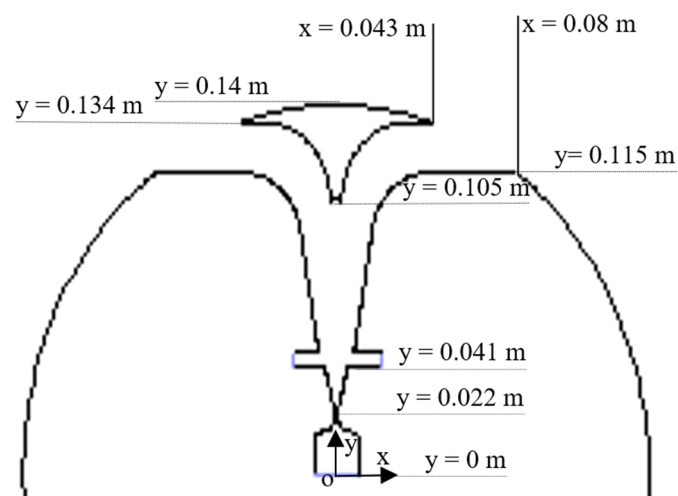
Figure 6. Geometric model of internal and external flow fields.
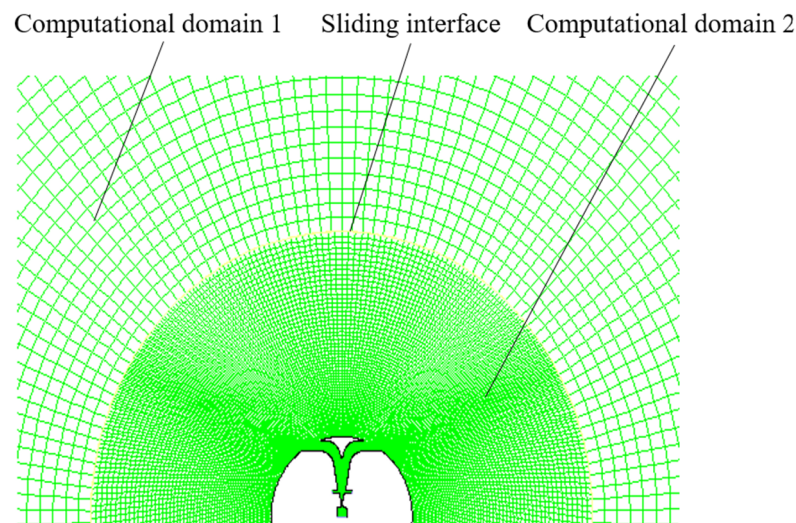
Figure 7. Internal and external flow field grid.

2.4. Computing Method

The computation in this paper was carried out in Fluent 16.1 software. The solver was the density-based solver. The spatial discrete scheme was the second-order upwind scheme. The flux scheme was Roe FDS format; the turbulence model selected was the RNG k–ε model. The material type was air (ideal gas). The Courant number was set to 2.

2.5. Numerical Method Validation

Table 1 lists the thrust values obtained through experiments and numerical simulation under different main gas source pressures, where P represents the air source pressure, F_{test} represents the resultant thrust value in the x direction measured through experiments, f_1 and f_r represent the calculated thrust values of the left and right nozzles in the x direction, and F represents the resultant thrust of f_1 and f_r. It can be seen that the relative error was within $\pm 5\%$, which suggests that the numerical method adopted in this paper is reliable.

Table 1. Calculated and experimental values of thrust.

P (MPa)	F_{test} (N)	f_r (N)	f_1(N)	F(N)
4	106.0	108.91	4.43	104.48
6	179.3	186.87	6.43	180.44
7	202.8	220.68	8.55	212.12
8	239.9	263.05	18.04	245.01
9	275.4	296.36	21.78	274.58

3. Results and Discussion

After considering the working characteristics of the supersonic jet element, the effects of the projectile rotation on the external control jet flow of a single supersonic jet element, the external control jet flow of two supersonic jet elements, and the internal and external flow fields of the whole supersonic jet element, were numerically simulated, and the effects of the projectile rotation on the working characteristics and internal and external flow fields of the supersonic jet element were comprehensively studied. The first two cases can be approximately assumed according to the working characteristics of the supersonic jet element: the impact of the projectile rotation on the single attitude control jet and the two parallel jets of attitude control jet.

In order to ensure the stability of the calculation, a lower speed was used initially, and then the speed was gradually increased to the required value. At the same time, the solution obtained at the lower speed was taken as the initial value for the calculation of the

flow field at a higher speed, so as to ensure the stability of the calculation and accelerate the convergence speed of the calculation.

3.1. Effect of Projectile Rotation on the External Jet Flow of a Single Supersonic Fluidic Element

The numerical simulation of a single attitude control jet in the rotating state was carried out for when the rotation angular velocity is 0 r/s, 5 r/s, 10 r/s and 20 r/s, respectively. The projectile rotates counterclockwise, which is reflected in the rotation of the flow field; that is, we see the clockwise rotation of the jet. Figure 8 shows the Mach number contours of the attitude control jet at different rotating speeds, and Figure 9 shows the total pressure at the axis of symmetry of the nozzle changes with the distance from the nozzle position at different rotating speeds. It can be seen that:

(1) When the rotational angular velocity is zero, the flow parameters are symmetrically distributed about the central axis, and the tangential velocity is symmetrically distributed on both sides of the jet centerline. After leaving the nozzle end face, a series of intersection and reflection phenomena of expansion wave and compression wave are formed near the nozzle outlet, and Mach reflection is formed on the centerline. Due to the effect of viscosity, the jet transfers momentum to the air flow on the left and right sides, producing two shear layers on the left and right sides. As the jet flows outward, the thickness of the shear layer increases and the momentum of the air flow in the middle region decreases.

(2) When the rotational angular velocity is greater than zero, the jet flow is asymmetric, and the asymmetry increases with the increase in the rotating speed. At this time, due to the influence of rotation, the jet is impacted by the external air flow, generating tangential momentum exchange, and forming a vortex surface on the rotating leeward side. The jet has an entrainment effect on the air on both sides. Because of the rotation, the jet absorbs more air on the rotating leeward side than on the rotating windward side, so the radial momentum exchange is large, with the result that the radial velocity at the edge of the rotating leeward side is smaller than that at the edge of the rotating windward side. The deflection degree of the jet near the projectile surface is less than that of the jet far away. This is because the radial momentum of the air flow near the missile body itself is relatively large, and the larger angular momentum is obtained from the rotation of the missile body, which makes the fluid micro cluster accelerate under the action of centrifugal force, resulting in smaller deflection curvature under the action of Coriolis force.

(3) The flow near the wall is driven by rotation, and the wall motion causes the forced vortex motion of the fluid with a high angular momentum and is thrown out along the radial direction. The jet flow shows the characteristics of strengthening at the axial line. This phenomenon is often referred to as "radial pumping" because the fluid is pumped outward along the radial direction by rotating the wall. This phenomenon is mainly caused by the momentum transport effect of the viscous boundary layer near the surface of the projectile and the centrifugal force.

(4) The flow law at low speed (10 r/s) has no obvious change compared with that at zero speed; with an increase in the rotation speed, the tangential velocity of each section increases, and the radius corresponding to the maximum tangential velocity also increases. The tangential velocity distribution under the rotation condition shows the characteristics of strengthening at the axis; when the rotating speed is increased from 10 r/s to 20 r/s, the flow law has fundamentally changed due to the strong effect of centrifugal force. Since the centrifugal force acting on the unit mass fluid micro cluster is equal everywhere on the cross section, the flow parameters change obviously along the height direction at high speed (>10 r/s).

(5) As the radius of the projectile body was 0.14 m for the calculation model, it can be seen from Figure 8 that the impact of rotation on jet flow is not obvious near the surface of the projectile body, but the impact of rotation cannot be ignored at a distance (greater than 0.3 m) from the surface of the projectile body; moreover, with the increase in rotating speed, the impact of rotation is closer to the surface of the projectile body. This is mainly because

the Coriolis force increases with the increase in rotating angular velocity, which makes the high momentum fluid near the wall also prone to track deflection.

(6) It can be seen that with the increase in rotational angular velocity, the jet incidence direction gradually deflects to the right, which is caused by the increase in tangential entrainment velocity at the jet inlet. This will cause thrust direction deflection and may affect thrust efficiency. This phenomenon is obvious only when the angular velocity is greater than 10 r/s.
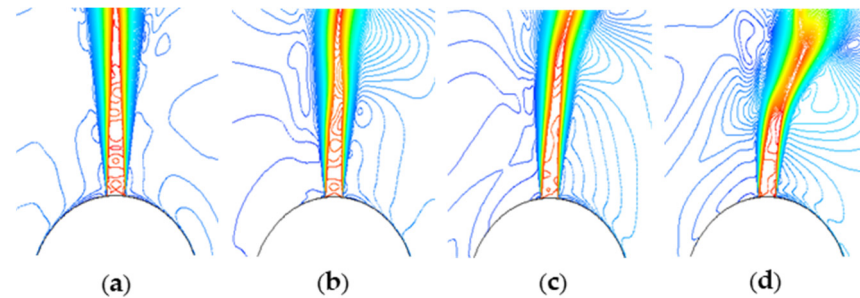
Figure 8. Mach number contours of external jet flow field at different rotational angular velocities: (**a**) 0 r/s, (**b**) 5 r/s, (**c**) 10 r/s, (**d**) 20 r/s.
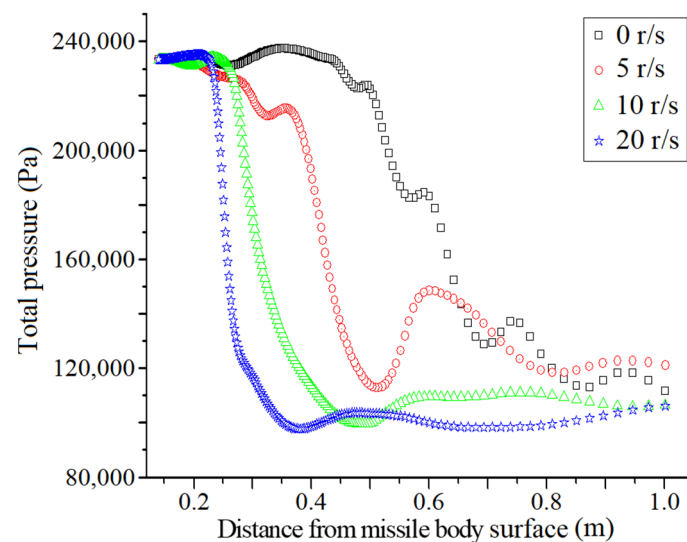
Figure 9. Diagram of total pressure at symmetrical axis of the jet changing with distance from nozzle exit.

To sum up, on the premise that the projectile diameter and nozzle size are fixed, the asymmetry of jet flow caused by rotation will directly affect the size and direction of attitude jet control force, and then affect the working efficiency of attitude control engine. By comparing the simulation results of different rotation angular rates, it can be seen that, under the same inlet conditions, with the increase in the rotation angular rate, the flow structure of the control jet flow field changes significantly, which causes the obvious change of the thrust vector, deflects the control thrust, effectively reduces the control thrust, thus affecting the stability and attitude control accuracy of the long-range rocket, and increases the gas consumption to a certain extent.

3.2. Effect of Projectile Rotation on the External Jet Flow of Two Supersonic Fluidic Elements

The numerical simulation of two parallel jets in the rotating state was carried out with the rotation angular velocity at 0 r/s, 5 r/s, 10 r/s and 20 r/s, respectively. The rotation direction of the projectile is counterclockwise, which means that the external flow field rotates clockwise with respect to the projectile. Figure 10 shows the Mach number contours at different rational speeds, Figure 11 shows the Mach number distribution at x-axis at

different rational speeds, and Figure 12 shows the static pressure distribution at x-axis at different rational speeds. It can be seen from the figures that:

(1) When the speed is zero, the flow parameters of the two jets in the Mach number contour map are symmetrically distributed with respect to the X axis. After leaving the nozzle end face, the two jets form a series of intersection and reflection phenomena of expansion wave and compression wave near the nozzle outlet, and form Mach reflection on the centerline.

(2) With the supersonic jet element working, the radius of the ejected gas entering the boundary increases, and the tangential velocity increases accordingly. Due to the existence of jet entrainment effect, both jets will deflect towards the vertical direction of the connection between the two nozzles and meet at a certain position, forming an approximate jet, and it can be clearly seen that a low-pressure vortex area is formed between the two jets.

(3) When the rotating speed is greater than zero, the symmetrical distribution of the flow parameters of the two jets about the x-axis is destroyed, and the flow field structure under rotating conditions shows obvious asymmetry. With the increase in rotating speed, this asymmetry becomes more obvious. The simulation results show that when the projectile has a certain rotation speed, the resultant force direction of the thrust vector generated by the two jets will no longer be parallel to the vertical line direction of the connecting line between the two exits, and the effective thrust will be reduced. Moreover, the control jet on the upper side is more affected by rotation than that on the lower side, and it deflects severely.

(4) As the calculation model had the projectile radius as 0.14 m, it can be seen from Figure 11 that with the increase in rotational angular velocity, the position where the maximum Mach number appears at the x-axis is closer to the projectile surface, but the maximum Mach number decreases. It can be seen from Figure 12 that when the speed is less than 10 r/s, the static pressure at the x-axis is almost not affected by rotation, but when the speed is 20 r/s, the effect of rotation cannot be ignored, so a conclusion similar to that in Section 3.1 can be obtained.
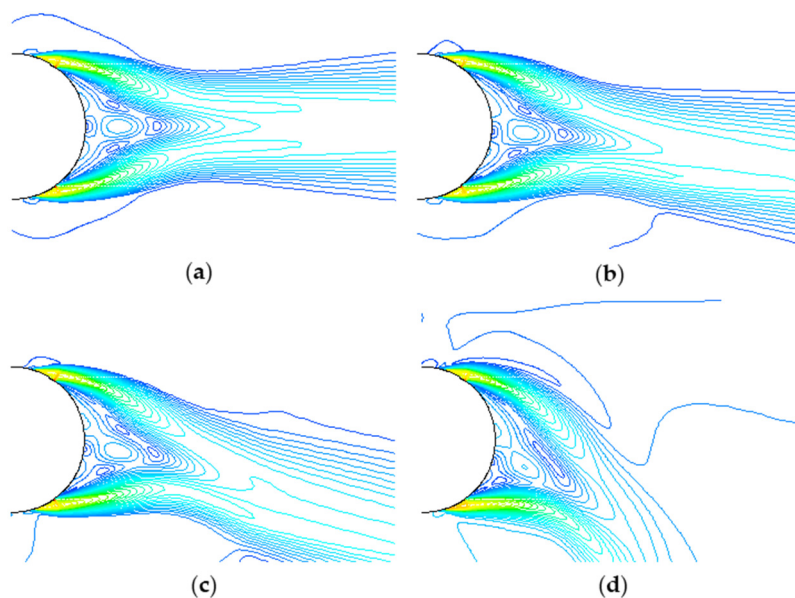
Figure 10. Mach number contours of two parallel external jets at different rotational angular velocities: (**a**) 0 r/s, (**b**) 5 r/s, (**c**) 10 r/s, (**d**) 20 r/s.
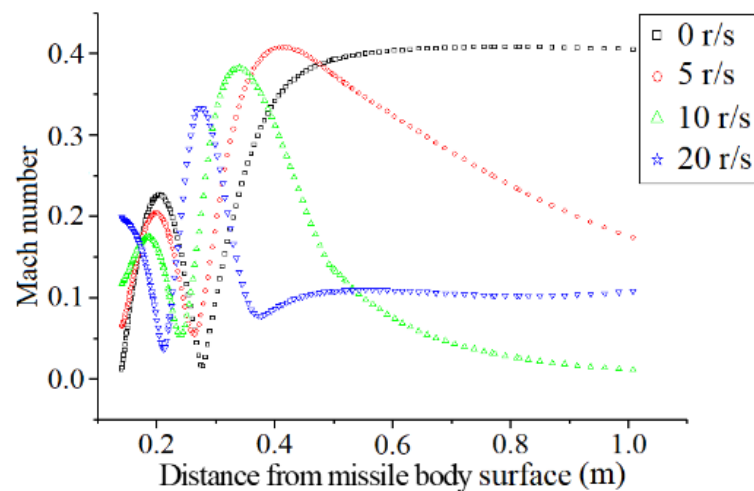
Figure 11. Mach number distribution at x-axis at different rotational angular velocities.
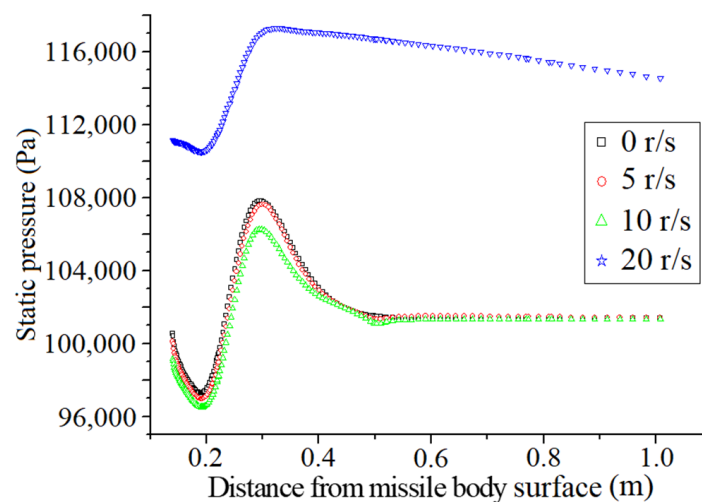
Figure 12. Static pressure distribution at x-axis at different rotational angular velocities.

3.3. Effect of Projectile Rotation on the Internal and External Flow Fields of the Supersonic Fluidic Element

The numerical simulation of internal and external flow fields of the supersonic fluidic element in the rotating state was carried out for when the rotational angular velocity is 0 r/s, 5 r/s, 10 r/s, 20 r/s and 50 r/s. The projectile rotates counterclockwise.

In order to analyze the influence of projectile rotation on the dynamic switching process of the supersonic fluidic element, the unsteady switching processes at different rotational angular velocities were simulated numerically. Table 2 shows the comparison of switching time at different rotating angular velocities, where Ω is the angular velocity, T is the switching time, and E is the deviation of the switching time from the situation of $\Omega = 0$. It can be seen from Table 1 that the switching time decreases with the increase in the rotating speed. However, the deviation of the switching time relative to the situation without rotation is obvious only when the rotating speed is large, and the order of magnitude of switching time deviation is within 10^{-4} s. When the rotating speed is lower than 50 r/s, the deviation of the switching time is less than 5%, so the projectile rotation has little influence on the switching time.

Table 2. Comparison of switching time at rotational angular velocity.

Ω (r/s)	T (ms)	E (%)
0	2.230	/
5	2.229	0.045
10	2.226	0.179
20	2.220	0.448
50	2.132	4.395

Figure 13 shows the contour of Mach number in the whole field at different rotational angular velocities. Figure 14 shows the contour of total pressure at different rotational angular velocities. It can be seen from Figure 13 that the rotation of the projectile does not change the basic flow mechanism of the internal flow field of the supersonic jet element. This suggests that the interior of the fluidic element can still attach to the wall and output normally when the projectile rotates.
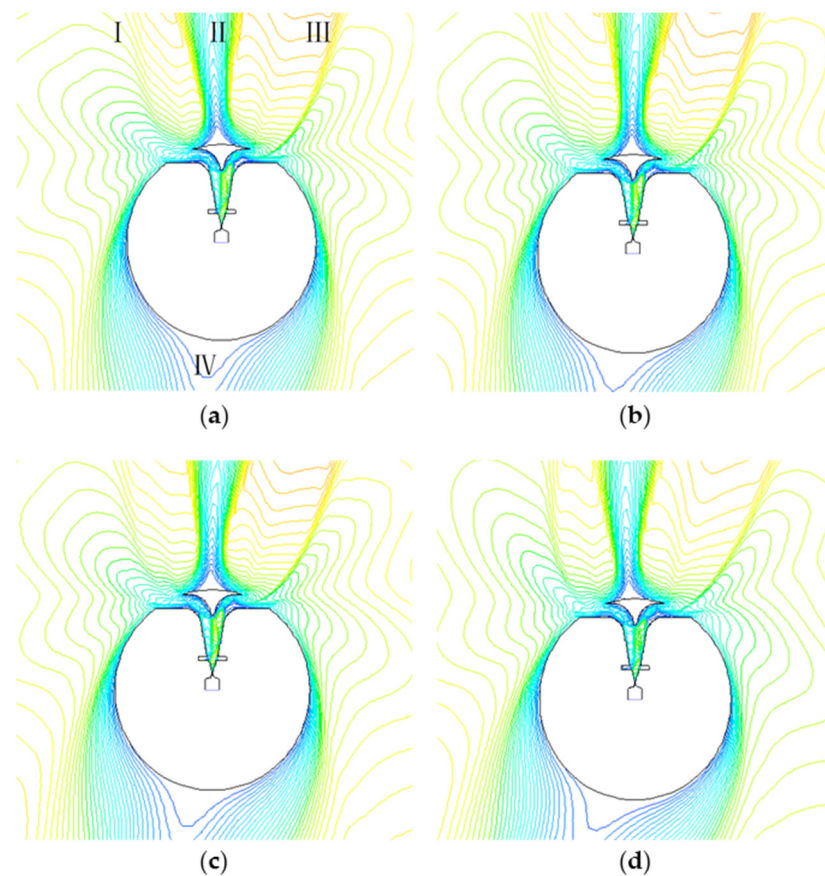
Figure 13. Mach number contours of the whole flow field at different rotational angular velocities: (**a**) 0 r/s, (**b**) 10 r/s, (**c**) 20 r/s, (**d**) 50 r/s.

It can be seen from Figures 13 and 14 that the effects of projectile rotation are mainly reflected in the following aspects: (1) The flows at I, II and III all deflect to the right with the increase in rotational angular velocity, which will make the effective thrust vector deflect clockwise; the low-pressure zone at position IV deflects to the left with the increase in rotational angular velocity. (2) The flow near the wall of the right nozzle at V is far away from the wall with the increase in rotational angular velocity, which will reduce wall friction and increases the thrust value in the x direction. This is mainly because the Coriolis force is large at a higher speed, which makes the air flow deviate from the wall to the right. If this effect is too significant, it may also cause the direction of outlet airflow to deflect. (3) With the increase in rotational angular velocity, due to the centrifugal effect, the wall-attachment

of flow at VI is delayed. It can be seen from the contour of total pressure that the above phenomenon is obvious when $\Omega = 50$ r/s, but not obvious when Ω is less than 20 r/s.

Figures 15 and 16 show the shear stress and density distributions on the right wall of the supersonic fluidic element at different rotational angular velocities. It can be seen from Figure 15 that when the rotational angular velocity is less than 20 r/s, the right-side wall-attachment point appears approximately at y = 0.0525 m, and the projectile rotation has little effect on the wall-attached flow. When the rotating speed is 50 r/s, the right-side wall-attachment point appears approximately at y = 0.054 m. The projectile rotation makes the wall-attachment point move backward. It can be seen that when the angular velocity is large, the attachment point moves backward obviously. This is mainly because the centrifugal force is relatively large at this time, leading to the tendency of the jet leaving the wall, which makes the jet attachment delay.

It can be seen from Figure 16 that the density distribution on the right wall at the angular velocity of 50 r/s is obviously different from that at the angular velocity less than 20 r/s. This is because at the angular velocity of 50 r/s, the centrifugal effect of internal flow is more obvious. When the location of the attachment point is pushed back, the area of the vortex zone at VI is significantly increased, and the pressure is reduced, causing the decrease in density. When the angular velocity is less than 20 r/s, the centrifugal effect in the internal flow field is not obvious. The disturbance from the external rotating flow field is introduced into the internal flow field from the left nozzle. With the increase in the angular velocity, the intensity of disturbance increases, so the density of the right wall will increase correspondingly, but the increase in amplitude is so small that it can be ignored.
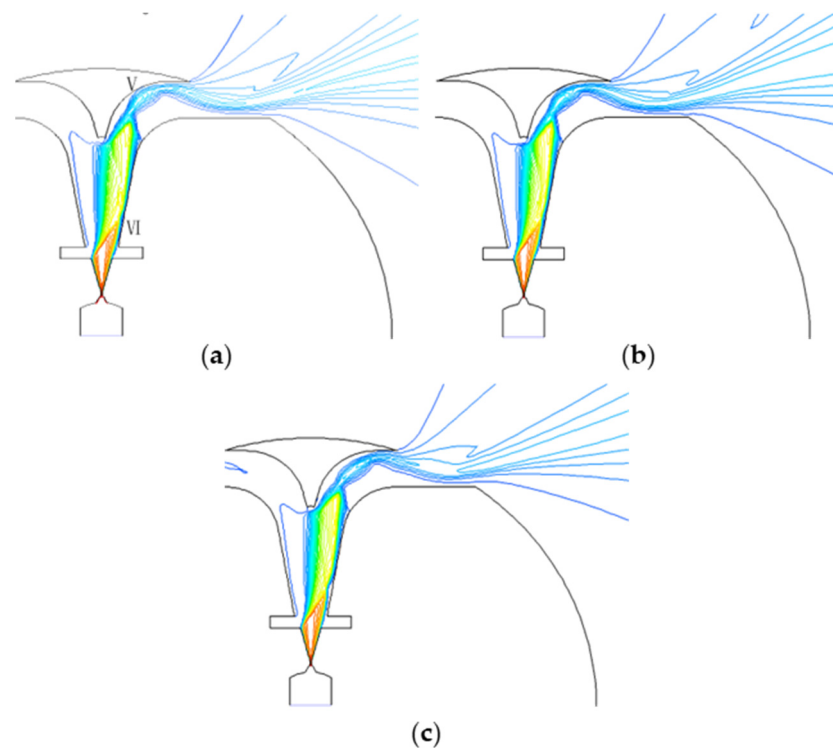
Figure 14. Total pressure contours at different rotational angular velocities: (**a**) 0 r/s, (**b**) 20 r/s, (**c**) 50 r/s.
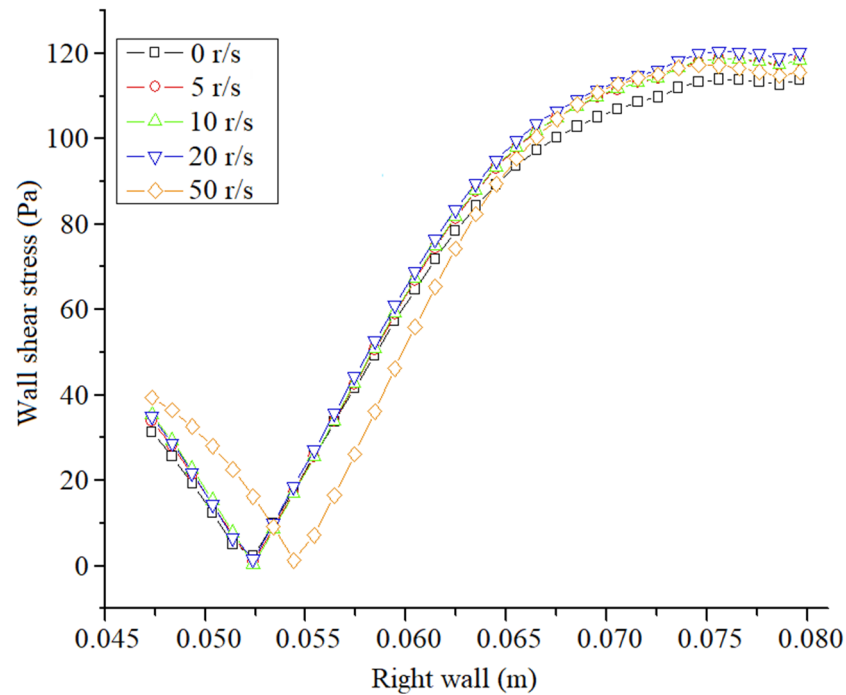
Figure 15. Distribution of shear stress on the right wall of supersonic fluidic element at different rotational angular velocities.
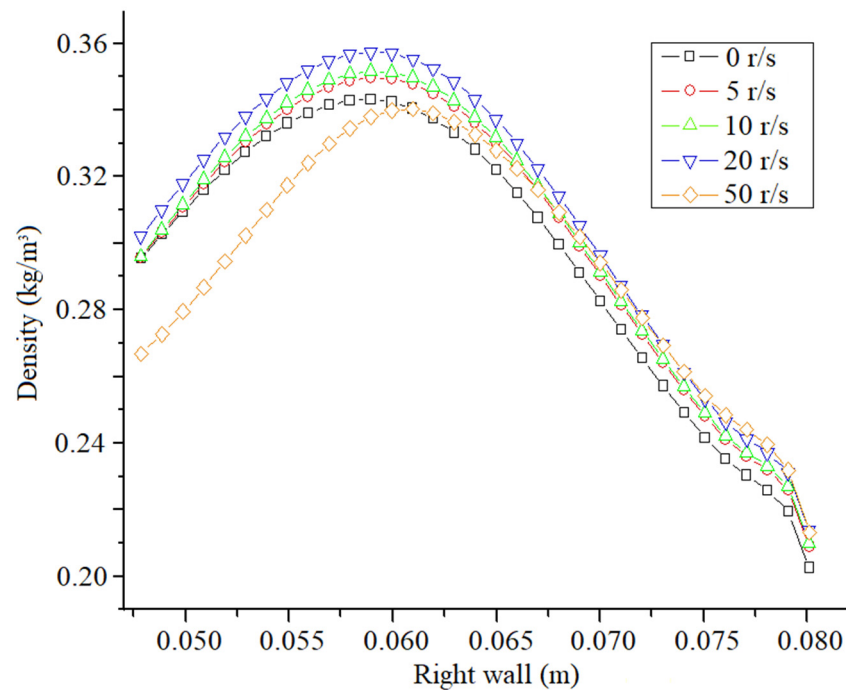
Figure 16. Density distribution of the right wall of the supersonic fluidic element at different rotational angular velocities.

Figure 17 shows the velocity distribution along the symmetric axis of the supersonic fluidic element at different rotational angular velocities. Figure 18 shows the temperature distribution along the symmetric axis of the supersonic fluidic element at different rotational angular velocities. The space of the axis from 0.00 m to 1.05 m refers to the internal flow field of the supersonic fluidic element and the space of the axis from 0.14 m to 0.3 m refers to the external flow field of the fluidic element. It can be seen from Figures 17 and 18 that between 0 and 0.09 m, the velocity and temperature distributions at different angular

velocities almost coincide. Between 0.09 m and 0.105 m, the temperature increases with the increase in angular velocity, while the velocity distributions at different angular velocities are almost coincident. Between 0.14 m and 0.3 m, which is in the external flow field area of the supersonic jet flow element, it can be clearly seen that the velocity and temperature distributions are completely different at different angular velocities. This result shows that rotation has little effect on the internal flow field structure within the possible rotational angular velocity range of the rocket projectile, while the rotation has obvious effects on the external flow field.
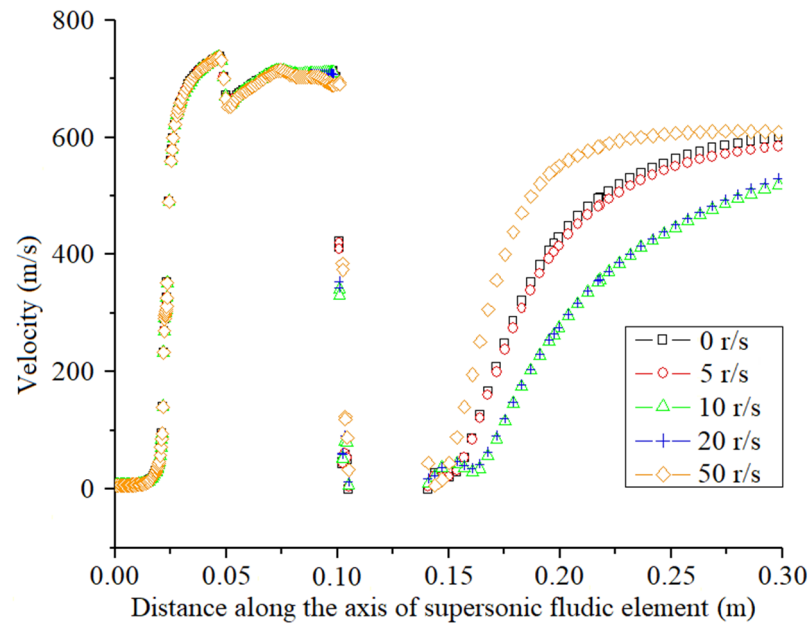
Figure 17. Velocity distribution along the symmetrical axis of supersonic fluidic elements at different rotational angular velocities.
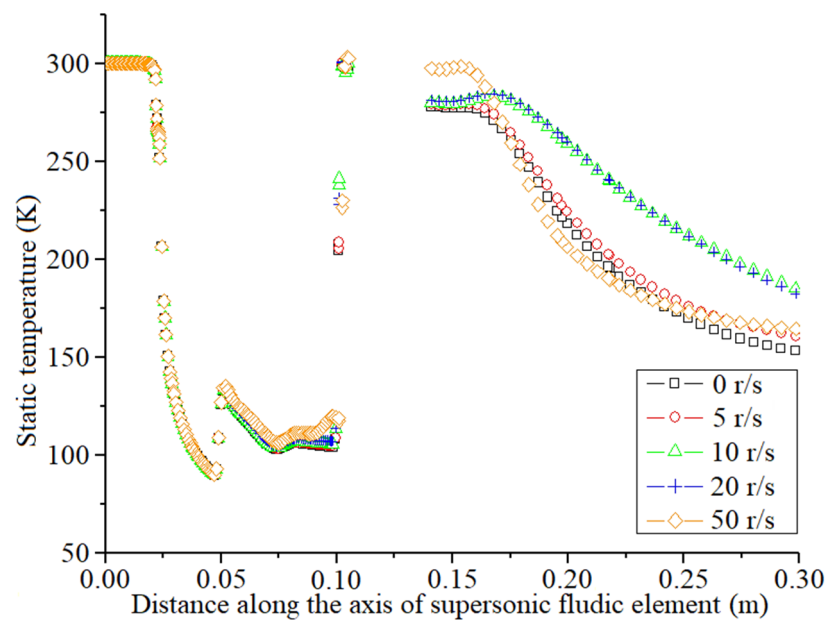
Figure 18. Temperature distribution along the symmetrical axis of supersonic fluidic elements at different rotational angular velocities.

Figure 19 shows the static pressure distribution of the right nozzle exit of the supersonic fluidic element at different rotational angular velocities. Figure 20 shows the thrust

distribution of the right nozzle exit of the supersonic fluidic element at different rotational angular velocities. It can be seen from Figures 19 and 20 that the output pressure and thrust curves at angular velocities less than 20 r/s almost coincide. With the increase in the angular velocity, the minimum pressure increases and the position of valley value moves outward, which shows that projectile rotation has an effect on the output pressure and the magnitude and direction of the thrust, but when the angular velocity is low, such as less than 20 r/s, this effect can be ignored. In Figure 19, it can be seen from the left and right ends of the curve that when the angular velocity reaches 50 r/s, the static pressure at the lower point of the right nozzle decreases and the static pressure at the upper end increases. This suggests that the airflow tends to flow towards the upper wall under the effect of centrifugal force. When the angular velocity is small, the centrifugal force is also small, and thus this effect is not obvious. It can be seen from Figure 20 that when the angular velocity is less than 20 r/s, all curves are basically coincident, suggesting that the thrust is basically not affected; when the angular velocity is 50 r/s, the thrust of the middle part increases significantly (about 20 N).

Figure 21 shows the static pressure distribution of the left nozzle exit of the supersonic fluidic element at different rotational angular velocities. Figure 22 shows the thrust distribution of the left nozzle exit of the supersonic fluidic element at different rotational angular velocities. It can be seen from Figures 21 and 22 that with the increase in angular velocity, the static pressure and thrust at the left nozzle exit slightly increases, which is caused by two reasons. The first reason is the centrifugal effect of internal flow. The second reason is that the ambient pressure at the left nozzle increases due to the influence of external rotating flow field. In general, this increase in the static pressure and thrust at the left nozzle exit is not very obvious and can be ignored. In Figure 22, when the angular velocity is less than 20 r/s, the curves basically coincide, indicating that the left thrust is little affected. When the angular velocity reaches 50 r/s, peak thrust at the left nozzle increases obviously. However, since the left thrust is inherently small, the contribution of this increase to the total thrust can be ignored.
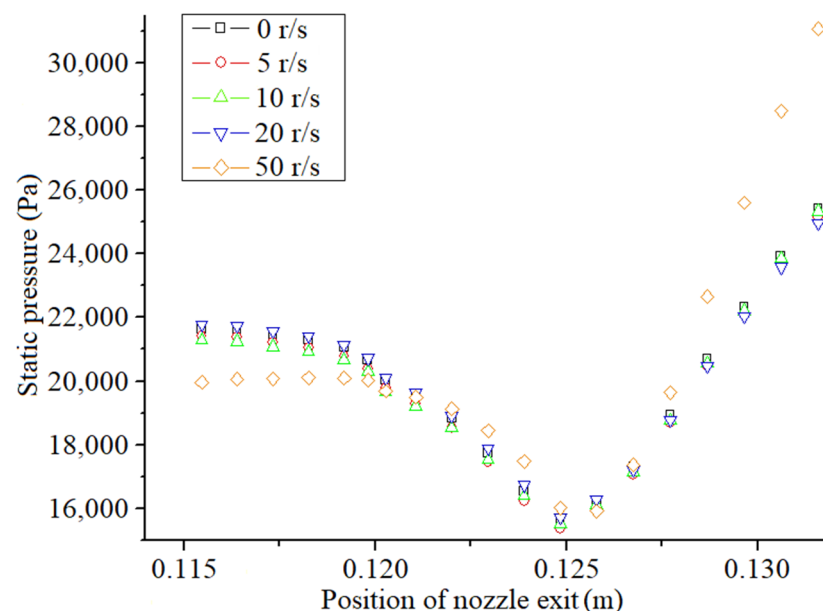
Figure 19. Static pressure distribution of the right nozzle exit at different rotational angular velocities.
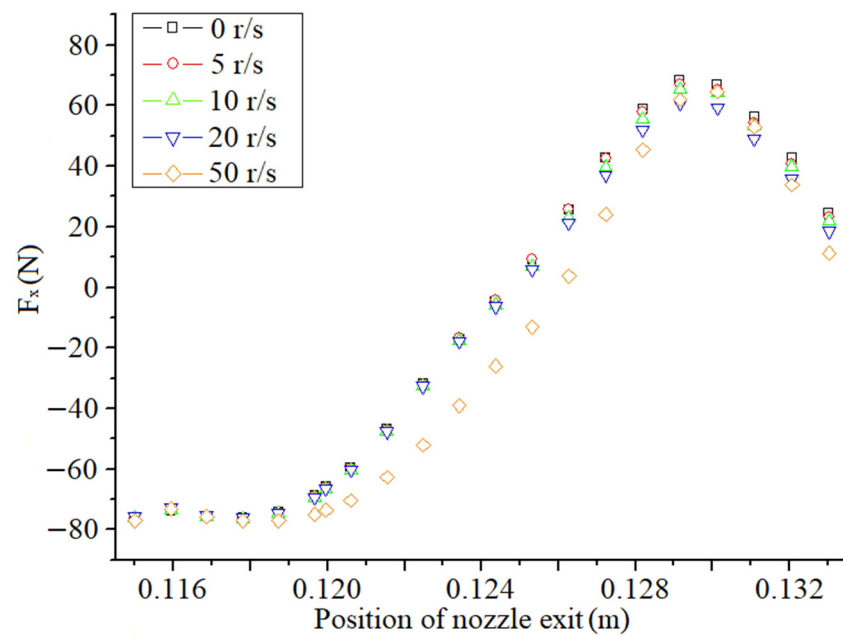
Figure 20. Thrust distribution along the right nozzle exit at different rotational angular velocities.
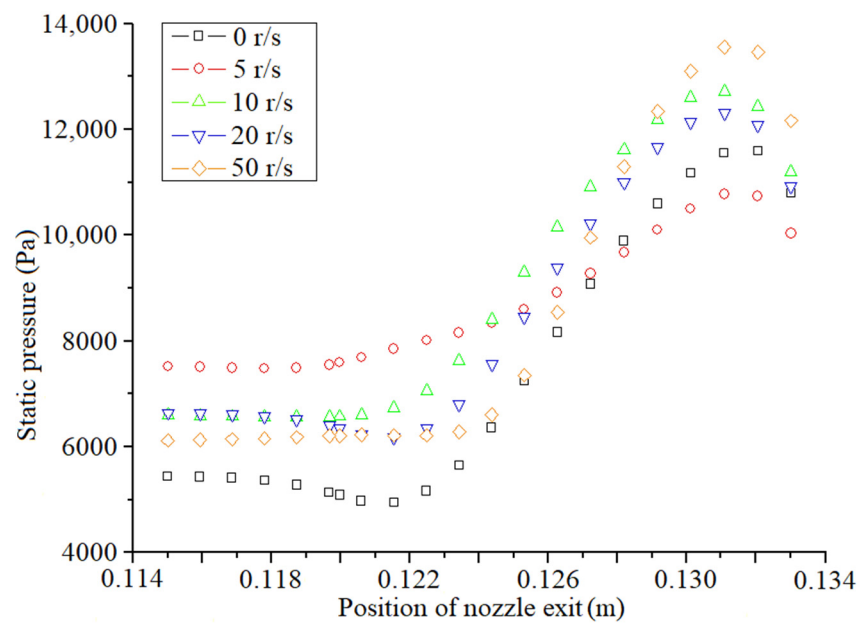
Figure 21. Static pressure distribution of the left nozzle exit at different rotational angular velocities.
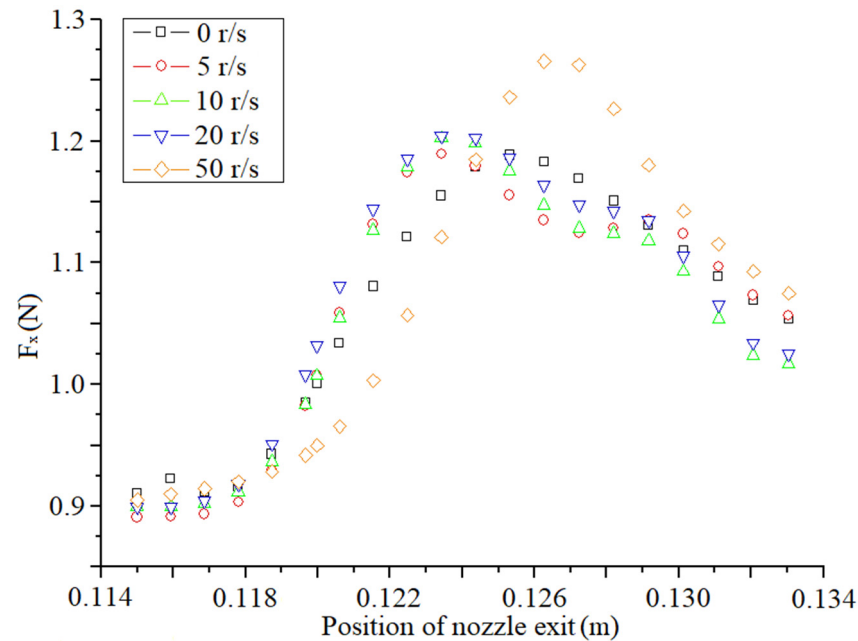
Figure 22. Thrust distribution along the left nozzle exit at different rotational angular velocities.

4. Conclusions

In this paper, the influence of projectile rotation on supersonic fluidic elements was studied by numerical method. It can be concluded from the numerical simulation results that:

(1) For the external flow field, the projectile rotation will cause asymmetry of the flow field and cause the outlet jet velocity to deflect to the right. The latter will deflect the effective thrust vector clockwise, thus affecting the effective thrust. The influence on outflow site is not obvious when the angular velocity is small (less than 10 r/s).

(2) The influence of projectile rotation on the internal flow field is weaker than that on the external flow field. The rotation of the projectile and rocket basically does not change the overall flow structure of the internal flow field. The main effects are to slightly delay the jet attachment to the wall and cause the air to flow in the right output channel slightly away from the upper wall, which is not obvious when the angular velocity is less than 20 r/s.

(3) With the increase in rotation angular velocity, the switching time of fluid components is shortened, but the change is not obvious. When the angular velocity is less than 50 r/s, the change of switching time is less than 5% compared with the situation when the missile body does not rotate.

(4) With the increase in angular velocity, the thrust of the middle part of the right nozzle exit increases, and the peak thrust at the left nozzle outlet increases slightly. The change of thrust distribution is not obvious when the angular velocity is less than 20 r/s.

Future research directions based on the subject of this paper are as follows:

(1) The optimization of structural parameters for supersonic fluidic elements to reduce the influence of missile body rotation and improve the working performance.

(2) Study of the comprehensive influence of multiple practical factors, such as projectile rotation, outflow field fluctuation and angle of attack, on the supersonic fluidic element.

(3) Study of the effects of multiphase flow and chemical reaction on the supersonic jet element under the condition that the main gas source ejects gas without full combustion.

Author Contributions: Conceptualization, Y.W.; methodology, Y.W.; software, Y.W.; validation, Y.W.; formal analysis, Y.W.; investigation, Y.W.; resources, Y.W.; data curation, Y.W.; writing—original draft preparation, N.W.; writing—review and editing, N.W. All authors have read and agreed to the published version of the manuscript.

References

1. Zhang, J.; Wang, Y.; Tan, J.; Zhu, G.; Liu, J. Numerical study of the switching mechanism of a jet valve using the meshless method. *Adv. Mech. Eng.* **2021**, *13*, 16878140211030066. [CrossRef]
2. Mair, M.; Bacic, M. Fluid Dynamics of a Bistable Diverter Under Ultrasonic Excitation—Part I: Performance Characteristic. *J. Fluids Eng.* **2021**, *143*, 071201. [CrossRef]
3. Mair, M.; Bacic, M.; Chakravarthy, K.; Williams, B. Fluid Dynamics of a Bistable Diverter Under Ultrasonic Excitation—Part II: Flow Visualization and Fundamental Mechanisms. *J. Fluids Eng.* **2021**, *143*, 071202. [CrossRef]
4. Schweitzer, T.; Hörmann, M.; Bühling, B.; Bobusch, B. Switching Action of a Bistable Fluidic Amplifier for Ultrasonic Testing. *Fluids* **2021**, *6*, 171. [CrossRef]
5. Bühling, B.; Strangfeld, C.; Maack, S.; Schweitzer, T. Experimental analysis of the acoustic field of an ultrasonic pulse induced by a fluidic switch. *J. Acoust. Soc. Am.* **2021**, *149*, 2150–2158. [CrossRef] [PubMed]
6. Park, S.; Ko, H.; Kang, M.; Lee, Y. Characteristics of a supersonic fluidic oscillator using design of experiment. *AIAA J.* **2020**, *58*, 2784–2789. [CrossRef]
7. Lee, E.; Cha, S.; Kwon, H.; Roh, T.; Lee, H. A Numerical Study on the Characteristics of Air–Fuel Mixing Using a Fluidic Oscillator in Supersonic Flow Fields. *Energies* **2019**, *12*, 4758. [CrossRef]
8. Reisch, U.; Meuer, R. CFD-simulation of the flow through a fluidic element. *Aerosp. Sci. Technol.* **2000**, *4*, 111–123. [CrossRef]
9. Bai, Y.; Ming, X. Numerical Simulation of Wall-Attached Jet Device. *J. Nanjing Univ. Aeronaut. Astronaut.* **2008**, *40*, 32–36.
10. Roger, R.; Chan, S. Numerical Study of Fluidic Bistable Amplifiers. In Proceedings of the Aiaa Fluid Dynamics Conference & Exhibit, Orlando, FL, USA, 23–26 June 2013.
11. Wang, N.; Xu, Y.; Zhang, G. Study of the Flow Structure in Supersonic Fluidic Element with Numerical Calculation Method. In Proceedings of the 2022 4th International Conference on Advances in Computer Technology, Suzhou, China, 22–24 April 2022.
12. Wang, N.; Xu, Y.; Zhang, G. Computational Investigation of the Internal Flow Characteristics of Supersonic Fluidic Element. In Proceedings of the 2022 4th International Conference on Advances in Computer Technology, Suzhou, China, 22–24 April 2022.
13. Murao, T.; Sudou, K. Numerical Analysis of the Behavior of the Jet in a Wall-Attachment Fluid Amplifier During the Switching Process. *Trans. Soc. Instrum. Control Eng.* **2009**, *36*, 364–366. [CrossRef]
14. Xu, Y.; Zhang, G.Q.; Wang, F. Numerical Simulation of the Viscous Flow for the Supersonic Jet Element. *Adv. Mater. Res.* **2011**, *189–193*, 2362–2365.
15. Xu, Y.; Zhang, G.Q. Influence of flow parameters on the dynamic performance for the supersonic jet element. *Acta Astronaut.* **2019**, *163*, 177–188. [CrossRef]
16. Xu, Y.; Zhang, G.Q.; Wang, F. Investigation of the unsteady flow for the supersonic jet element. *Adv. Mater. Res.* **2011**, *201–203*, 2178–2181. [CrossRef]
17. Xu, Y.; Zhang, G.Q. Switching mechanism investigation for the supersonic jet element: Deflection, attachment and adjustment stages. *Acta Astronaut.* **2019**, *163*, 208–224. [CrossRef]
18. Xu, Y.; Zhang, G.Q. Numerical investigation of switching mechanism for the supersonic jet element. *Acta Astronaut.* **2017**, *136*, 342–353. [CrossRef]
19. Yong, X. The Flow Simulation in the Fluidic Amplifier. *Open Autom. Control Syst. J.* **2011**, *3*, 8–12.
20. Yong, X.; Yang, S.; Bo, M. Three dimension numerical simulation of a jet device control channel. *Chin. J. Comput. Mech.* **2002**, *19*, 31–35.
21. Sun, N.; Wang, J.; Ma, X.; Niu, L. Influence Factors of Light-Small Supersonic Fluidic Element on Performance. *J. Propuls. Technol.* **2019**, *40*, 525–531.
22. Peng, J.M.; Yin, Q.L.; Li, G.L.; Liu, H.; Wang, W. The effect of actuator parameters on the critical flow velocity of a fluidic amplifier. *Appl. Math. Model.* **2013**, *37*, 7741–7751. [CrossRef]
23. Peng, J.M.; Zhang, Q.; Li, G.L.; Chen, J.W.; Gan, X.; He, J.F. Effect of geometric parameters of the bistable fluidic amplifier in the liquid-jet hammer on its threshold flow velocity. *Comput. Fluids* **2013**, *82*, 38–49. [CrossRef]
24. Peng, Z.; Yao, X. The Modeling and Simulation of a Kind of Jet Elements. *J. Proj. Rocket. Missiles Guid.* **2009**, *29*, 52–54.
25. Zhang, Z.B.; Wu-Ju, M.A. Simulation and Test of a Kind of Jet Element. *Comput. Simul.* **2016**, *33*, 76–79.
26. Wuju, M.; Xia, Q. The Effect of Jet Element Switch Time on Guidance Precision of Spinning Missile. *J. Proj. Rocket. Missiles Guid.* **2013**, *33*, 5–7.

27. Anderson, J.D.; Wendt, J. *Computational Fluid Dynamic*; McGraw-Hill: New York, NY, USA, 1995; pp. 83–88.
28. Abraham, J.; Magi, V. *Computations of Transient Jets: RNG k-e Model versus Standard k-e Model*; Technical Report; SAE International: Warrendale, PA, USA, 1997. [CrossRef]